Journal of Molecular Catalysis A: Chemical 330 (2010) 112–120

Contents lists available at ScienceDirect

Journal of Molecular Catalysis A: Chemical

journal homepage: www.elsevier.com/locate/molcata

Deactivation studies of Fischer–Tropsch synthesis on nano-structured iron catalyst

Ali Nakhaei Pour[a,b,*], Mohammad Reza Housaindokht[a], Sayyed Faramarz Tayyari[a], Jamshid Zarkesh[b], Mohammad Reza Alaei[b]

[a] Department of Chemistry, Ferdowsi University of Mashhad, P.O. Box 91775-1436, Mashhad, Iran
[b] Research Institute of Petroleum Industry of National Iranian Oil Company, P.O. Box 14665-137, Tehran, Iran

ARTICLE INFO

Article history:
Received 1 December 2009
Received in revised form 26 June 2010
Accepted 20 July 2010
Available online 30 July 2010

Keywords:
Fischer–Tropsch synthesis
Iron-based catalyst
Catalyst deactivation
Nano-sized particles
Microemulsion

ABSTRACT

Deactivation kinetics of bulk and nano-structured microemulsion prepared iron catalysts were studied in Fischer–Tropsch synthesis (FTS), from fitting of data to a generalized power-law expression (GPLE), $r_d = k_d (a - a_\infty)^m$. Conventional bulk iron catalyst was prepared by general bulk co-precipitation method and nano-structured iron catalyst was prepared by microemulsion method. A deactivation model involving parallel paths is proposed, i.e. simultaneous conversion of (a) atomic to polymeric to graphitic carbon and (b) active carbon-rich carbides to inactive carbon-poor carbides. Compositions of bulk iron phase and phase transformations of carbonaceous species during catalyst deactivation in FTS reaction were characterized by temperature-programmed surface reaction with hydrogen (TPSR-H_2), XRD and TEM techniques.

1. Introduction

Iron-based catalysts are preferred for Fischer–Tropsch synthesis (FTS) utilizing synthesis gas derived from coal or biomass because of the excellent activity for the water–gas shift reaction, which allows using a synthesis gas with a low H_2/CO ratio directly without an upstream shift-step [1–4]. But it is well known that low product selectivity, catalyst agglomeration and sintering limit the use of iron catalysts in high temperate operation [5–8]. Activity of iron-based FTS catalysts changed during their operation because of sintering of metal particles, coke formation, poison deposition and solid state transformation [6–8]. It is important in design of iron-based FT catalysts to achieve a clear understanding of carbon species deposition and phase transformation of iron catalyst during different pretreatments and under industrial FTS conditions. Results of previous studies have shown that the formation of surface carbides is required before the catalyst can exhibit high activity [9–11]. However, the correlation between bulk carbide species, surface carbon species, and catalytic activity has not yet been established. It is well known that the distribution of iron phases in the catalyst changes during time-on-stream [12,13]. Although the active phase for the FTS reaction is still in debate, the oxidation of the metallic iron and/or the iron carbide phases is believed as one of the factors for catalyst deactivation. H_2O (the primary product in the FTS reaction) and CO_2 (which produced from water–gas shift reaction) is usually considered as an oxidizing agents for iron phases [14,15]. Apart from the oxidation of the iron phases, several authors have pointed out the importance of a graphite-like carbonaceous compound on the deactivation of the iron catalysts [16–18]. Coke formation results from undesired side reactions and affects the intrinsic activity through the coverage of sites and the blockage of pores [6–8].

Xu and Bartholomew [19] identified and quantified several carbon and metal carbide species on the surface of unsupported and supported used iron catalysts by means of temperature-programmed surface reaction with hydrogen (TPSR-H_2). In both systems, good correlation between coverage of atomic surface carbon species and catalyst performance was found. Herranz et al. [13] studied the effect of pretreatment condition on active phase formation during the activation of iron catalyst. They reported that only metallic iron was formed when the pretreatment is performed with hydrogen. However, iron carbide, mainly cementite and the Hägg carbide are formed with CO (pure or diluted) and/or syngas pretreatments. In our previous work, the effects of Ca, Mg and La promoters on the activity and products selectivity of iron catalysts were studied during FTS performance [20–22]. These results showed that the catalyst deactivation is increased with increas-

* Corresponding author at: Research Institute of Petroleum Industry of National Iranian Oil Company, P.O. Box 14665-137, Tehran, Iran. Tel.: +98 21 44739716; fax: +98 21 44739716.
E-mail addresses: nakhaeipoura@ripi.ir, nakhaeipoura@yahoo.com (A. Nakhaei Pour).

1381-1169/$ – see front matter © 2010 Elsevier B.V. All rights reserved.
doi:10.1016/j.molcata.2010.07.010

ing the catalyst surface basicity via formation of inactive carbon (graphitic) and lower active iron carbide (cementite).

Poisoning involves species that are present in the feedstock and irreversibly adsorb or modify the active sites through chemical reactions. The poison may also be formed in the reactor from feedstock components or intermediates. Since in this study, precautions were taken to eliminate sulfur impurities in the feed, the observed deactivation was not as result of sulfur poisoning clearly.

Recent studies showed that nano-sized iron particles played an essential role to achieve high FTS activity [22–33]. Some authors, prepared supported iron-based Fischer–Tropsch catalysts by microemulsion, reported high activity and marked selectivity to oxygenate. In our previous works, the effects of nano-sized iron particles on catalyst structure, surface area, reduction and carburization, textural properties, and activity behavior of precipitated Fe/Cu/La catalyst in a fixed bed reactor has been studied [29–32].

Whereas kinetic equations for the main reactions are now well recognized as an essential tool for process design and simulation, kinetic modeling of coke formation and catalyst deactivation is still considered too complicated to be dealt with along the lines commonly accepted and used for the main reactions. As a result, oversimplified empirical equations with limited validity are derived from experimental work generally scheduled too late in the development of the process.

The present study evaluates the variety of the catalyst activity and deactivation manner and also developed a kinetic modeling for catalyst deactivation of nano-structured iron catalyst with time-on-stream. Consequently, a detailed characterization study of deactivation kinetics and the nature of the bulk and surface species formed in nano-sized iron particles during FTS reaction was performed in the present work. Effects of nano-sized iron particles in carbonaceous species were studied on the surface of the iron catalysts by XRD and temperature-programmed surface reaction with hydrogen (TPSR-H_2) after pretreatment and FTS reaction. The characterization results were correlated with the catalytic activity measurements.

2. Experimental

2.1. Catalyst preparation

The Fe/Cu/La catalysts were prepared via two processing routes, bulk precipitation and microemulsion. Bulk catalyst was prepared by co-precipitation of Fe and Cu nitrates at a constant pH to form porous Fe/Cu oxyhydroxide powders that was promoted by impregnation with $La(NO_3)_3$ precursor after treatment in air, as described previously [20,21].

The nano-structured catalyst precursors were prepared by co-precipitation in a water-in-oil microemulsion as described previously [29–33]. In the same way as in the bulk case, precipitation experiments of Fe/Cu/La catalyst precursors in microemulsion system were carried out in the same semi-batch reactor. The precipitation was performed in the single-phase microemulsion operating region. For this purpose, a water solution of metal precursors, $Fe(NO_3)_3{\cdot}9H_2O$ (Fluka puriss, p.a. ACS: 98–100%) and $Cu(NO_3)_2{\cdot}4H_2O$ (Fluka, purum, p.a. >97%) was added to a mixture of an oil phase (chloroform, Aldrich, >99%) and the commercial sodium dodecyl sulfate (SDS) surfactants. Besides, 1-butanol as a co-surfactant was added to system in order to obtain a proper microemulsion. Lanthanum promoter was added by wet impregnation method with $La(NO_3)_3$ precursor on its optimal value after treatment in air as described previously [20]. The promoted catalysts were dried at 383 K for 16 h and calcined at 773 K for 3 h in air. The catalyst compositions were designed in terms of the atomic ratios as: 100Fe/5.64Cu/2La.

2.2. Catalyst characterization

The oxide precursors as well as the catalysts after pretreatment and FTS reaction were characterized by XRD and TPSR-H_2. In our previous work, a complete characterization of catalysts was described [29,30]. X-ray diffraction (XRD) spectra of fresh catalysts were collected with a Philips PW1840 X-ray diffractometer using monochromatized Cu (Kα) radiation to determine catalyst phases after calcinations, pretreatment and FTS reaction. For determine catalyst phases after pretreatment and FTS reaction, the samples were passivated with an 1 vol.% O_2/He mixture at room temperature for 1 h according to a standard procedure described elsewhere [13,34]. Then the samples were analyzed by X-ray diffraction (XRD) and different species detected from the XRD analysis according to the JCPDS cards. The characteristic peak at $2\theta = 33.3^\circ$ corresponds to the hematite 104 plane was used to calculate the average metal particle size by the Scherrer equation.

The morphology of prepared catalysts was observed with a transmission electron microscope (TEM, LEO 912 AB, Germany). An appropriate amount of Fe_2O_3 suspension directly taken from the reaction solution was dropped onto the carbon-coated copper grids for TEM observation. The average particle size (d_{TEM}) and particle size distribution were determined by TEM images with counting more than 100 particles.

For the temperature-programmed surface reaction with hydrogen (TPSR-H_2) ca. 0.5 g of the sample was loaded into a U-shaped quartz reactor. The samples were pretreated in a 5% (v/v) H_2/N_2 gas mixture with space velocity of 15.1 nl h^{-1} g_{Fe}^{-1} at 0.1 MPa by increasing temperature from ambient to 673 K with 5 K/min, then maintained for 1 h and subsequently reduced to 543 K. The activation was followed by the synthesis gas stream with $H_2/CO = 1$ and space velocity of 3.07 nl h^{-1} g_{Fe}^{-1} for 24 h in 0.1 MPa and 543 K and then flushed with Ar at 543 K until the baseline leveled off (ensuring complete removal of adsorbed species on the reduced catalyst surface). Then the samples were cooled to room temperature under Ar flow for TPSR-H_2 test. The reactivity of the species remained on the surface of the solids was tested by H_2/Ar (10%) flow. The gas flow rate was 50–100 ml/min, and the temperature was increased from 300 to 1100 K at a linear heating rate of 5 K/min. The outlet of the microreactor was pass from a condenser and zeolite trap to remove liquefied phases (especially water), then connected to a Shimadzu 4C gas chromatograph equipped with two subsequent connected packed columns: Porapak Q and Molecular Sieve 5A, and a thermal conductivity detector (TCD) with argon which was used as a carrier gas for hydrogen and CH_4 analysis.

For evaluation of catalysts after FTS reaction, the samples were flushed with Ar at 543 K until the baseline leveled off (ensuring complete removal of adsorbed species on the reduced catalyst surface). Then the samples were cooled to room temperature under Ar flow for (TPSR-H_2) tests. The reactivity of the species remaining on the surface of the solids was tested by passing H_2/Ar (10%). The gas flow rate was 50–100 ml/min, and the temperature was increased from 300 to 1100 K at a linear heating rate of 5 K/min. The outlet of the microreactor were passed from a condenser and zeolite trap to remove liquid phases, and then connected to a Shimadzu 4C gas chromatograph.

2.3. Catalytic performance

Steady-state FTS reaction rates were measured in a continuous spinning basket reactor (stainless steel, $H = 0.122$ m, $D_0 = 0.052$ m, $D_i = 0.046$ m) with temperature controllers (WEST series 3800). A J-type movable thermocouple made it possible to monitor the bed temperature axially, which was within ± 0.5 K of the average bed temperature. The reactor system also included a 50 cm^3 stainless steel cold trap at ambient temperature located before the gas chro-

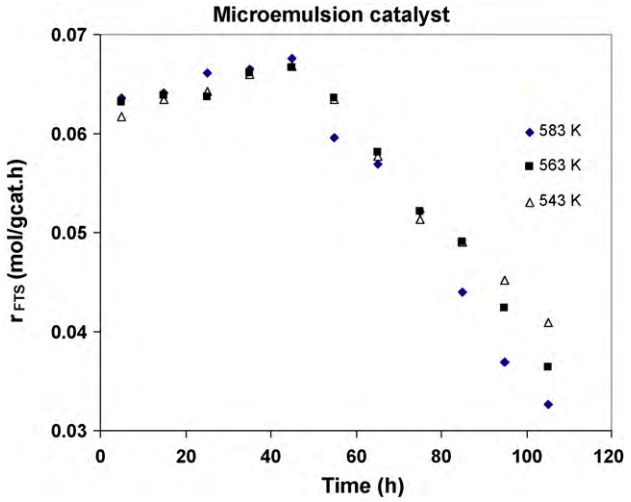

Fig. 1. FTS reaction rates versus time for microemulsion nano-structured iron catalyst. Reaction conditions: $P_{H_2}/P_{CO} = 1$, 1.7 MPa, SV = 4.9 nl h^{-1} g_{Fe}^{-1}.

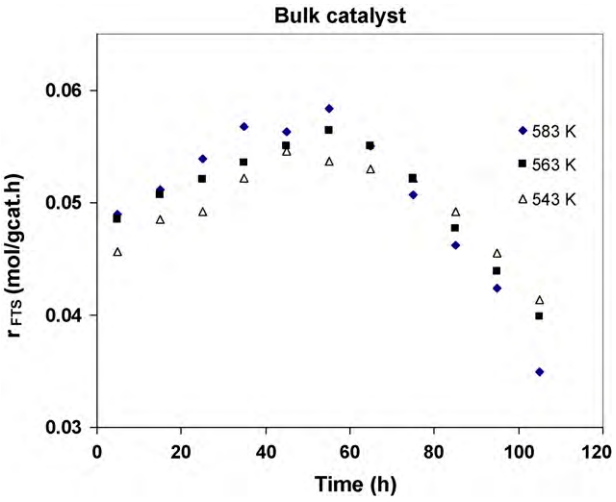

Fig. 2. FTS reaction rates versus time for bulk iron catalyst. Reaction conditions: $P_{H_2}/P_{CO} = 1$, 1.7 MPa, SV = 4.9 nl h^{-1} g_{Fe}^{-1}.

matograph sampling valve. Non-condensable gases were passed through sampling valve into an online gas chromatograph continuously then vent through a soap-film bubble meter. Separate Brooks 5850 mass flow controllers were used to add H_2 and CO at the desired rate to admixing vessel that was preceded by a palladium trap and a molecular sieve trap to remove metal carbonyls and water before entering to the reactor. A compact pressure controller was used to control the pressure. The flow rate of tail gas is measured by a wet test gas meter.

Blank experiments show that the spinning basket reactor charged with inert silica sand without the catalyst has no conversion of syngas. The fresh catalyst is crushed and sieved to particles with the diameter of 0.25–0.36 mm (40–60 ASTM mesh). The weight of the catalyst loaded is 2.5 g and diluted by 30 cm^3 inert silica sand with the same mesh size range. The catalyst samples were activated by a 5% (v/v) H_2/N_2 gas mixture with space velocity 15.1 nl h^{-1} g_{Fe}^{-1} at 0.1 Mpa and 1800 rpm. The reactor temperature increased to 673 K with a heating rate of 5 K/min, maintained for 1 h at this temperature, and then reduced to 543 K. The activation is followed by the synthesis gas stream with $H_2/CO = 1$ and space velocity 3.07 nl h^{-1} g_{Fe}^{-1} for 24 h in 0.1 MPa and 543 K before setting the actual reaction condition. After catalyst reduction, synthesis gas was fed to the reactor at conditions operated at 543, 563 and 583 K, 1.7 MPa, (H_2/CO) feed = 1 and a space velocity equal to 4.9 nl h^{-1} g_{Fe}^{-1}.

The products were analyzed by means of three gas chromatographs, a Shimadzu 4C gas chromatograph equipped with two subsequent connected packed columns: Porapak Q and Molecular Sieve 5A, and a thermal conductivity detector (TCD) with Ar as carrier gas for hydrogen analyzing. A Varian CP 3800 with a chromosorb column and a thermal conductivity detector (TCD) were used for CO, CO_2, CH_4, and other non-condensable gases. A Varian CP 3800 with a Petrocol™ DH100 fused silica capillary column and a flame ionization detector (FID) were used for organic liquid products so that a complete product distribution could be provided.

3. Results

3.1. Deactivation kinetic

FTS reaction rates versus time-on-stream (TOS) at 1.7 Mpa, H_2/CO partial pressure ratio equal to1, space velocity 4.9 nl h^{-1} g_{Fe}^{-1}, and 543, 563 and 583 K are shown in Figs. 1 and 2 for microemulsion and bulk catalysts, respectively. FTS reaction rate can be calculated as:

$$r_{FTS} = r_{CO} - r_{CO_2} \quad (1)$$

where r_{CO_2} is the rate of CO_2 formation and r_{CO} is the rate of CO consumption. As shown in these figures nano-structured iron catalyst shows higher initial activity in comparison with bulk catalyst. The rate of catalyst deactivation (r_d) is defined as the rate of decrease of the activity a (i.e., rate at time t divided by the rate at which the catalyst activity is considered to be one), over with time and can be determined separately:

$$r_d = \frac{da}{dt} \quad (2)$$

where the normalized activity (a) can be considered as:

$$a = \frac{r_{FTS}}{r_{FTS_0}} \quad (3)$$

where r_{FTS} refers to the FTS rate at time t and $r_{FTS(0)}$ refers to the FTS rate for un-deactivated condition (before 45 h in Fig. 1 and 55 h in Fig. 2).

Normalized activity–time plots are provided in Figs. 3 and 4 for bulk and microemulsion (nano-structured) catalysts. It is evident

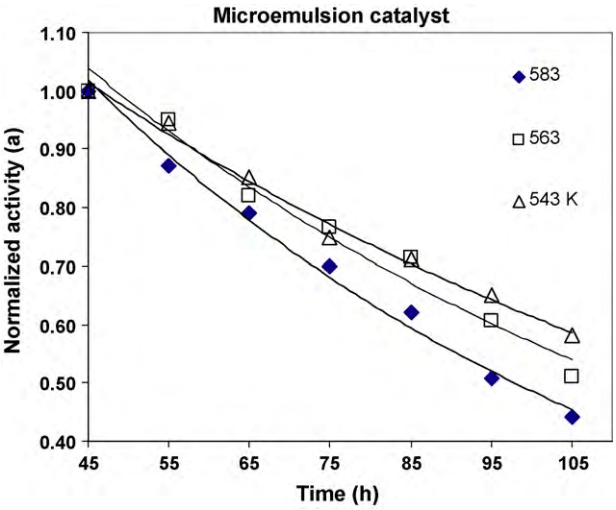

Fig. 3. Normalized activity, versus time for microemulsion nano-structured iron catalyst. Reaction conditions: $P_{H_2}/P_{CO} = 1$, 1.7 MPa, SV = 4.9 nl h^{-1} g_{Fe}^{-1}.

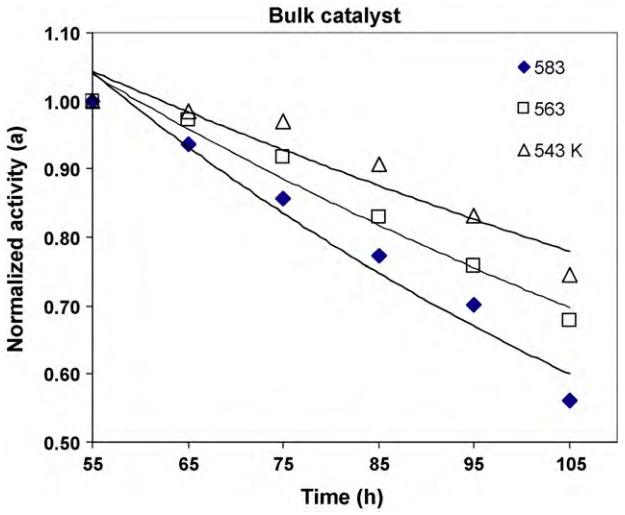

Fig. 4. Normalized activity, versus time for bulk iron catalyst. Reaction conditions: $P_{H_2}/P_{CO} = 1$, 1.7 MPa, SV = 4.9 nl h^{-1} g_{Fe}^{-1}.

from these plots that the extent of deactivation increases as the temperature increases. As shown in these figures, the FTS activity and deactivation manner of bulk catalyst more sensitive to temperate than microemulsion catalyst. The rate of deactivation depends on the temperature and the activation energy of the processed reaction as deactivation rate constant (k_d). Also, deactivation rates depend on the rate of decrease of the activity ($a - a_\infty$) where a is the activity, and a_∞ is the activity at infinite reaction time, the partial pressures of the deactivating component P_d as $f(a, P_d)$:

$$-r_d = k_d f(a, p_d) \tag{4}$$

A generalized power-law expression (GPLE) is the appropriate rate form for deactivation phenomena in which normalized activity approaches an asymptotic value at long times [7]:

$$-r_d = -\frac{da}{dt} = k_d p_d^m (a - a_\infty)^n \tag{5}$$

Since the dependence of deactivation rate on H_2 and CO partial pressures was observed to be relatively secondary compared to the dependencies on activity and temperature, the data were fitted to a simplified, concentration-independent GPLE:

$$-r_d = -\frac{da}{dt} = k'_d (a - a_\infty)^n \tag{6}$$

where $k_d p_d^m$ is replaced by k'_d. A deactivation order n of unity was found to fit the data well for both catalysts. The dependency of the reaction rate parameters on temperature is described by the Arrhenius equation. The activation energy is determined using the Arrhenius equation that directly introduced into the kinetic parameters:

$$k_d = k_{d\infty} \exp\left(\frac{-E_A}{RT}\right) \tag{7}$$

Hence, a plot of $\ln(k)$ versus $1/T$ should give a straight line with slope of $-E_A/R$.

Values of the deactivation rate constant k_d at various temperature and activation energies for deactivation rates were determined and listed in Table 1 for bulk and microemulsion catalysts. Values of 49 and 35 kJ/mol are obtained for bulk and nano-structured catalysts, respectively. It is evident that deactivation rates constant (Table 1) are significantly larger for nano-structured relative to the bulk catalyst means that the nano-structured catalyst shows higher deactivation rates.

Table 1
FTS deactivation kinetics data. Reaction conditions: $H_2/CO = 1$, 1.7 MPa, SV = 4.9 nl h^{-1} g_{Fe}^{-1}..

Catalyst	k_d (h^{-1})			E_a (kJ/mol)
	543 K	563 K	583 K	
Bulk catalyst	0.011	0.017	0.022	49
Microemulsion catalyst	0.018	0.026	0.031	35

3.2. Crystalline structure in fresh catalyst, after pretreatment and FTS reaction

Nano-structure and conventional iron catalysts characterized by X-ray diffraction (XRD) measurement after calcination. Fig. 5 shows the XRD patterns of iron catalysts prepared by the microemulsion and bulk technology. From this Fig., the characteristic peaks corresponding to (0 1 2), (1 0 4), (1 1 0), (1 1 3), (0 2 4), (1 1 6), (0 1 8), (2 1 4), (3 0 0) planes are located at $2\theta = 24.3^\circ$, 33.3°, 35.8°, 40.8°, 49.6°, 54.1°, 57.6°, 64.1° and 65.6°, respectively. They show very close to the ones with cubic hematite structured Fe_2O_3 crystal in JCPDS database. Diffraction data indicate that the presence of lanthanum and copper and then subsequent treatment in dried air did not influence the hematite crystalline phases detected by X-ray diffractions in different catalyst preparation methods. It shows that the hematite structure once formed remains stable during subsequent aqueous impregnation and thermal treatment. Consequently, the crystalline phases of all samples demonstrate the cubic hematite structured Fe_2O_3 crystal, no matter what kind of preparation method (bulk or microemulsion) is involved. This strongly infers that microemulsion system cans only modules physical properties of reaction medium but without changing the reaction paths and arrangements of crystal structure. It is worthily to notice that the corresponding peaks in microemulsion systems are much broader than those in bulk system. This is obviously attributed to the smallest particles are obtained in microemulsion system. The characteristic peak at $2\theta = 33.3^\circ$ corresponds to the hematite 104 plane was used to calculate the average metal particle size by the Scherrer equation. The calculated d_{XRD} for the samples were determined 38.3 and 23.8 nm for bulk conventional and nano-structured catalysts, respectively.

X-ray powder diffraction patterns (XRD) of the passivated pretreated samples is illustrated in Fig. 6. A summary of the different species detected from the XRD analysis (according to the JCPDS card) after the pretreatments is listed in Table 2. Before the XRD analysis, the catalysts were passivated in 1% O_2/He stream at room temperature. As shown in Fig. 6, a broad diffraction peak is observed at ca. 44° in their XRD profiles irrespective of the iron carbides. In reduction and carbidation procedure, iron oxide was trans-

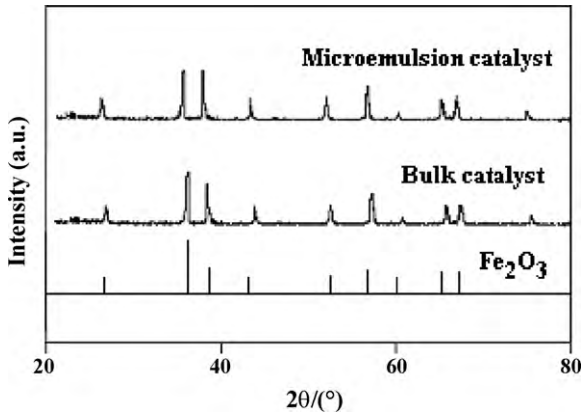

Fig. 5. X-ray powder diffraction patterns of the fresh catalysts.

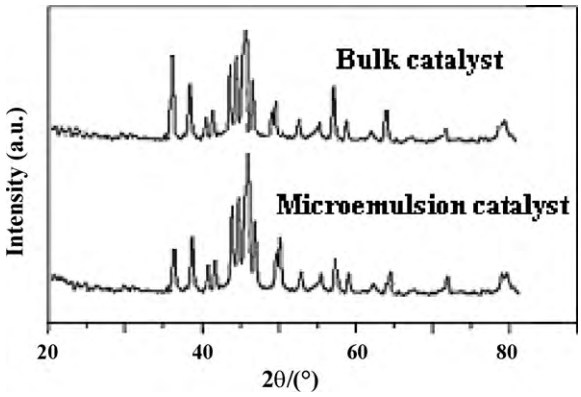

Fig. 6. X-ray powder diffraction patterns of the passivated catalysts after pretreatment. Before the measurements, the catalysts were passivated in 1% O_2/He stream at room temperature.

formed from $Fe_2O_3 \rightarrow Fe_3O_4 \rightarrow \alpha$-Fe → iron carbide. α-Fe could not be observed in our reduced catalyst because the metallic iron was fairly reactive to dissociated carbon from carbon monoxide. Among the iron carbides, O carbides (carbides with carbon atoms in octahedral interstices, ε-Fe_2C and $\acute{\varepsilon}$-$Fe_{2.2}C$) and TP carbides (carbides with carbon atoms in trigonal prismatic interstices, χ-$Fe_{2.5}C$ and θ-Fe_3C) have been identified [12,13]. The assignment of the different Fe carbide phases ($\acute{\varepsilon}$-$Fe_{2.2}C$, cementite carbide (θ-Fe_3C) and Hägg carbide (χ-$Fe_{2.5}C$)) from the X-ray diffractograms performed carefully because they showed similar diffraction patterns. According to the JCPDS card, only $\acute{\varepsilon}$-$Fe_{2.2}C$ shows a main diffraction peak near 43° among these carbides [14]. Furthermore, peaks at ca. 39° and 41° use to identify Hägg carbide (χ-$Fe_{2.5}C$) (JCPDS 36-1248). Peak assignments are based on the characteristic angles of cementite carbide (χ-Fe_3C) (JCPDS 76-1877) at 78.0° and 70.1°, which are not present in the θ-$Fe_{2.5}C$ pattern [13]. On the contrary, sharp peaks are clearly observed at 35°, 57° and 63° as well in the diffraction profiles are assigned to Fe_3O_4. The relative intensity of the diffraction peaks was taken into account for the identification of the carbide species.

As shown in Fig. 3 and Table 2, the nano-catalyst has higher amounts of carbon-rich $\acute{\varepsilon}$-carbides than the conventional catalyst that has more iron-rich χ and θ phases. These results attribute to lower size of iron crystals that increases the chance of contacts between carbon monoxide and the bulk iron in pretreatments of catalysts and converts bulk iron to more carbon-rich $\acute{\varepsilon}$-$Fe_{2.2}C$ carbides. Pervious results suggest that the most catalytic active phase in FTS is $\acute{\varepsilon}$-carbide ($Fe_{2.2}C$) which converts into the Hägg carbide (χ-$Fe_{2.5}C$) and subsequently changes into the cementite (θ-Fe_3C) with lower carbon content, under FTS conditions [8,9,35].

Fig. 7 shows XRD pattern of samples after 105 h time-on-stream (TOS) in FTS reaction. Before the XRD measurements, the catalyst

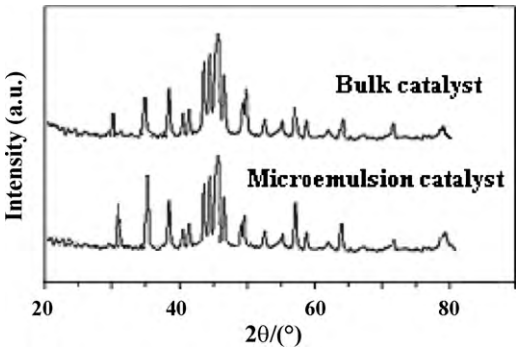

Fig. 7. X-ray powder diffraction profiles of the catalysts after the FTS reaction. Reaction conditions: 563 K, H_2/CO = 1, 1.7 MPa, SV = 4.9 nl h^{-1} g_{Fe}^{-1}, TOS = 105 h.

was passivated in 1% O_2/He stream at room temperature. Also, a summary of different species detected from the XRD analysis after FTS reaction is listed in Table 3. As shown in Fig. 7 and Table 3, the nano-catalyst has high amounts of the cementite carbides (θ-Fe_3C) and magnetite (Fe_3O_4) after reaction than bulk one. As shown in this figure and Table 3, conversely with pretreatment results, the nano-catalyst has higher amounts of the cementite carbides (θ-Fe_3C) and magnetite (Fe_3O_4). These results attribute to higher initial activity of nano-catalyst (Figs. 1–4) that increases the concentration of oxidized products (H_2O and CO_2) in reaction atmosphere, converts $\acute{\varepsilon}$-$Fe_{2.2}C$ carbides into the Hägg carbide (χ-$Fe_{2.5}C$) and subsequently transforms into the cementite (θ-Fe_3C) with lower carbon content and magnetite (Fe_3O_4) [6–8]. Therefore, the oxidation of the Fe carbides by H_2O (the primary product in the FTS reaction) and CO_2 (produced via water–gas shift reaction) is more significant on this catalyst.

3.3. Temperature-programmed surface with hydrogen (TPSR-H_2) reaction of catalysts after pretreatment and FTS reaction

Carbonaceous surface species in catalysts was studied by temperature-programmed surface reaction with hydrogen (TPSR-H_2) after pretreatment and/or FTS reaction. A method for qualities and quantitative analysis of overlapping TPSR-H_2 peaks for iron-based FT catalyst was reported by Bartholomew et al. [6,19].

Bartholomew et al. [6,19] have identified up to six different carbonaceous species onto the surface of iron-based catalysts under the FTS reaction. The reactivity of these species was assigned from the temperature value of the methane formation peak in the TPSR-H_2; that is, the more reactive the species, the lower formation temperature. The identified species (in order of reactivity) were $C_\alpha > C_\beta > C_\gamma > C_\delta$. Two different C_γ and C_δ species were reported. C_α is the atomic carbonaceous species resulting from the dissociative adsorption of CO; C_β is a polymeric (2–3 atoms) surface carbona-

Table 2
Phase detected by XRD in catalysts after pretreatment.

Catalyst	Phases detected	Fe-carbides/Fe_3O_4 ratio	$\acute{\varepsilon}$-$Fe_{2.2}C$/(θ-Fe_3C, χ-$Fe_{2.5}C$) ratio
Bulk catalyst	Fe_3O_4, θ-Fe_3C, χ-$Fe_{2.5}C$, $\acute{\varepsilon}$-$Fe_{2.2}C$	2.4	1.3
Microemulsion catalyst	Fe_3O_4, θ-Fe_3C, χ-$Fe_{2.5}C$, $\acute{\varepsilon}$-$Fe_{2.2}C$	3.5	2.1

χ-$Fe_{2.5}C$: Hägg carbide, θ-Fe_3C: cementite carbide and Fe_3O_4: magnetite.

Table 3
Phase detected by XRD in catalysts after 105 h FTS reaction.

Catalyst	Phases detected	Fe-carbides/Fe_3O_4 ratio	θ-Fe_3C/χ-$Fe_{2.5}C$ ratio
Bulk catalyst	Fe_3O_4, θ-Fe_3C, χ-$Fe_{2.5}C$	5.5	2.3
Microemulsion catalyst	Fe_3O_4, θ-Fe_3C, χ-$Fe_{2.5}C$	3.6	3.4

χ-$Fe_{2.5}C$: Hägg carbide, θ-Fe_3C: cementite carbide and Fe_3O_4: magnetite. Reaction conditions: 563 K, H_2/CO = 1, 1.7 MPa, SV = 4.9 nl h^{-1} g_{Fe}^{-1}.

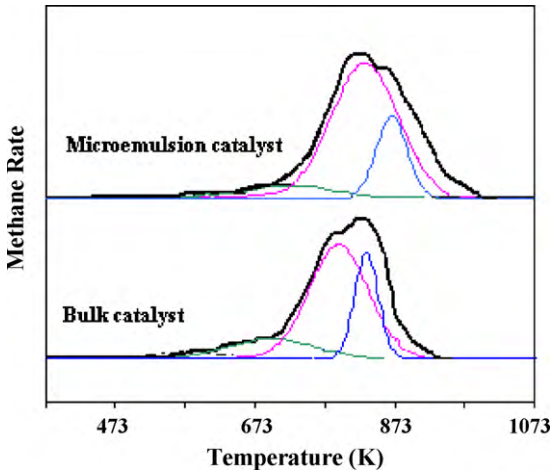

Fig. 8. Temperature-programmed surface reaction with hydrogen (TPSR-H_2) of the catalysts after pretreatment. Before the measurements, the catalysts were passivated in 1% O_2/He stream at room temperature.

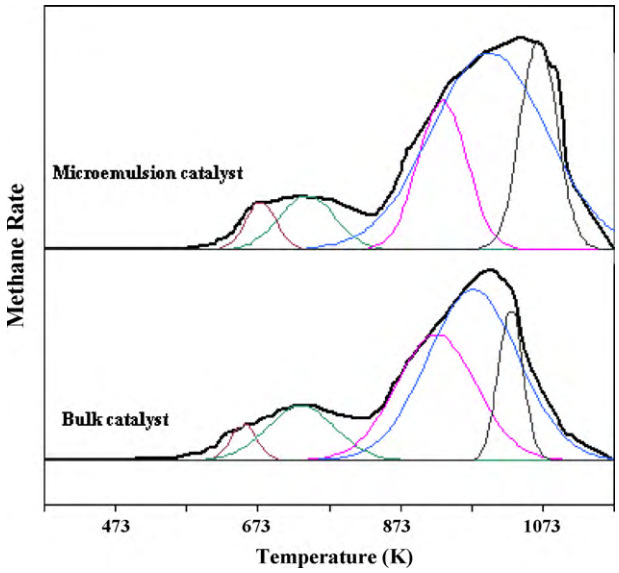

Fig. 9. Temperature-programmed surface reaction with hydrogen (TPSR-H_2) of the catalysts after FTS reaction. Reaction conditions: 563 K, H_2/CO = 1, 1.7 MPa, SV = 4.9 nl h^{-1} g_{Fe}^{-1}, TOS = 105 h.

ceous species. C_γ is the iron carbide, and C_δ is the graphite-type carbonaceous species that are both ordered and less ordered.

TPSR-H_2 spectra, which shows methane evolution rate (due to reaction of carbon with H_2), are plotted in Fig. 8 for pretreatment catalysts. The spectra were deconvoluted and fitted with Gaussian curves to yield up to four peaks. Designed as α, β, γ_1, and γ_2 species are assigned to atomic carbon (carbidic), amorphous surface methyl chains or films, and bulk iron carbides.

Peak temperatures increase in order of decreasing reactivity with H_2, and assignments for the species are based on previous literature [13,19].

Table 4 listed the peak temperatures and the corresponding percentage compositions of carbon species for samples after pretreatment. It should be emphasized that during pretreatment no graphitic carbon is observed. Based on Bartholomew et al. [6,7,19] results, we concluded that carbides γ_1 attributed to $\acute{\varepsilon}$-$Fe_{2.2}C$ and carbides γ_2 related to Hägg (χ-$Fe_{2.5}C$) and cementite (θ-Fe_3C) carbides. The calculated amounts of these carbides in Table 4 are similar to XRD results. These results show that formation of α-carbon and transformation of α-carbons to carbide form, enhanced when the catalyst particle size decreased from bulk to microemulsion catalyst, because of increasing CO content on surface of catalyst.

Xu, and Bartholomew [19] showed that the C_α/C_β ratio are depended to H_2 content on surface of catalyst and this ratio enhances while H_2 content increases. Previous results [28] shows that when the catalyst crystal size decreases from conventional to nano-structure catalyst, the concentration of the adsorbed hydrogen on the catalyst surface increases, and change of C_α/C_β ratio in this trend assigned to this fact.

TPSR-H_2 results for carbonaceous surface species in catalyst after 105 h FTS reaction are shown in Fig. 9 and listed in Table 5. Because of some dramatic effects of the Soxhlet wax extraction on carbonaceous species, which is reported by Xu and Bartholomew [19], dewaxation of catalysts after reaction is not considered. The carbon equivalents for α-carbon (the most reactive carbon form) and carbides trends for the catalyst are similar to pretreatments results but the carbide composition and amounts of graphitic carbon changed. Based on XRD results, γ_1 and γ_2 carbons attribute to Hägg (χ-$Fe_{2.5}C$) and cementite (θ-Fe_3C) carbides, respectively. This is due to absence of $\acute{\varepsilon}$-$Fe_{2.2}C$ carbides after FTS reaction.

As shown in Fig. 6 and Table 5, the γ_2/γ_1 carbons ratio (which relate to cementite θ-Fe_3C carbides/Hägg, χ-$Fe_{2.5}C$ carbides ratio) in nano-structure catalyst is higher than conventional catalyst after FTS reaction. Similar results were shown in XRD pattern treatment of used catalysts. This fact attributes to higher initial activity of this catalyst that enhanced the concentration of oxidizing products (H_2O and CO_2) in reaction atmosphere, and increased the

Table 4
Temperature-programmed surface reaction with hydrogen (TPSR-H_2) results of carbonaceous species after pretreatments.

Catalyst	Carbidic α		Amorphous β		Carbide γ_1		Carbide γ_2	
	P.T	C.C	P.T	C.C	P.T	C.C	P.T	C.C
Bulk catalyst	568	1.1	696	12.2	793	49.9	833	36.8
Microemulsion catalyst	547	3.1	693	15.1	800	55.4	838	26.4

P.T: peak temperature (K) and C.C: compositions of carbon species (mol%).

Table 5
Temperature-programmed surface reaction with hydrogen (TPSR-H_2) results of carbonaceous species after 105 h FTS reaction.

Catalyst	Carbidic α		Amorphous β		Carbide γ_1		Carbide γ_2		Graphitic δ	
	P.T	C.C	P.T	C.C	P.T	C.C	P.T	C.C	P.T	C.C
Bulk catalyst	613	2.7	716	8.6	851	23.1	896	53.0	1000	12.6
Microemulsion catalyst	610	3.1	717	8.5	865	15.9	930	54.0	1005	18.5

P.T: peak temperature (K). C.C: compositions of carbon species (mol%). Reaction conditions: 563 K, H_2/CO = 1, 1.7 MPa, SV = 4.9 nl h^{-1} g_{Fe}^{-1}.

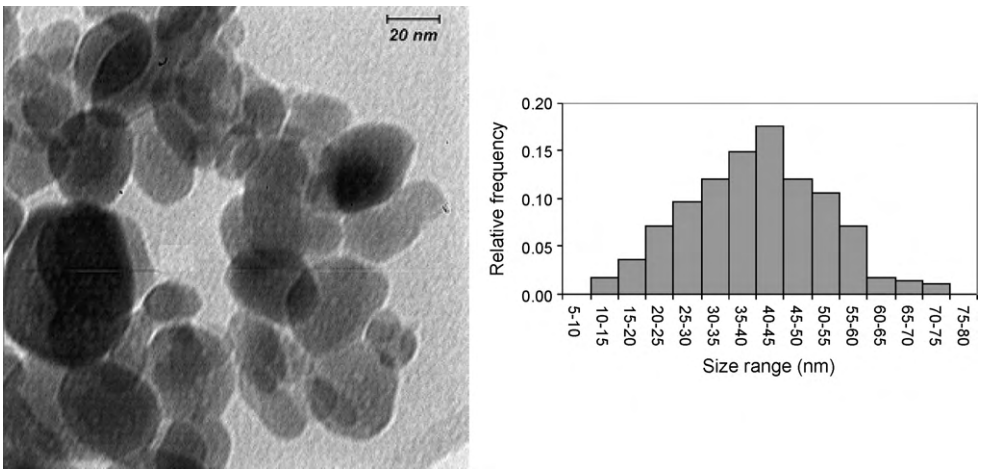

Fig. 10. TEM image and relative particle size distribution of bulk catalyst samples before reaction.

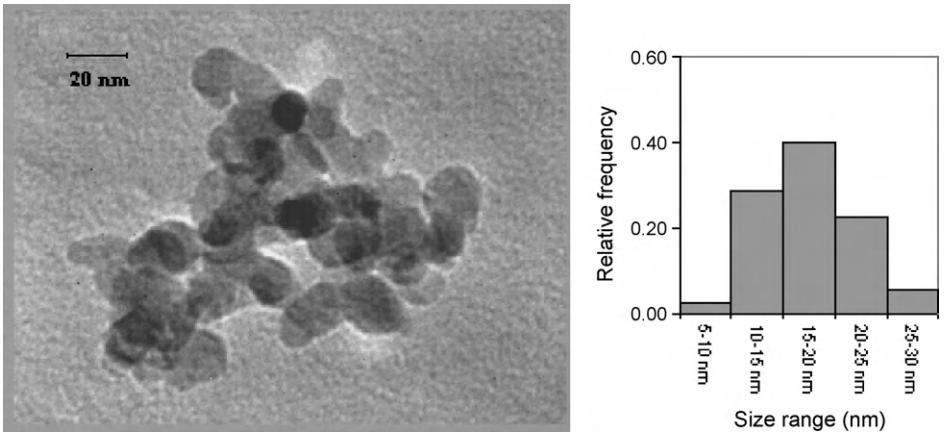

Fig. 11. TEM image and relative particle size distribution of microemulsion catalyst samples before reaction.

rate of $\acute{\varepsilon}$-$Fe_{2.2}C \rightarrow \chi$-$Fe_{2.5}C \rightarrow \theta$-$Fe_3C$ conversion. It is apparent from Table 5 that amounts of graphitic carbon in used catalysts for nano-structure catalyst are higher than conventional catalyst.

3.4. Particle size growth of catalysts particles

During activation and FTS, the gas composition in contact with the catalyst has the potential to exhibit either reducing or oxidizing properties. Also, a variety of iron carbide/oxide phase may be evolved during the activation/synthesis process. Thus there exists a strong possibility that the catalyst particles may undergo growth in size depending on the process condition.

The TEM images and particle size distribution of the catalysts are shown in Figs. 10 and 11 for conventional bulk and nano-structured catalysts, respectively. The initial size of the microemulsion nano-catalyst was in the narrow range of 10–20 nm but this results

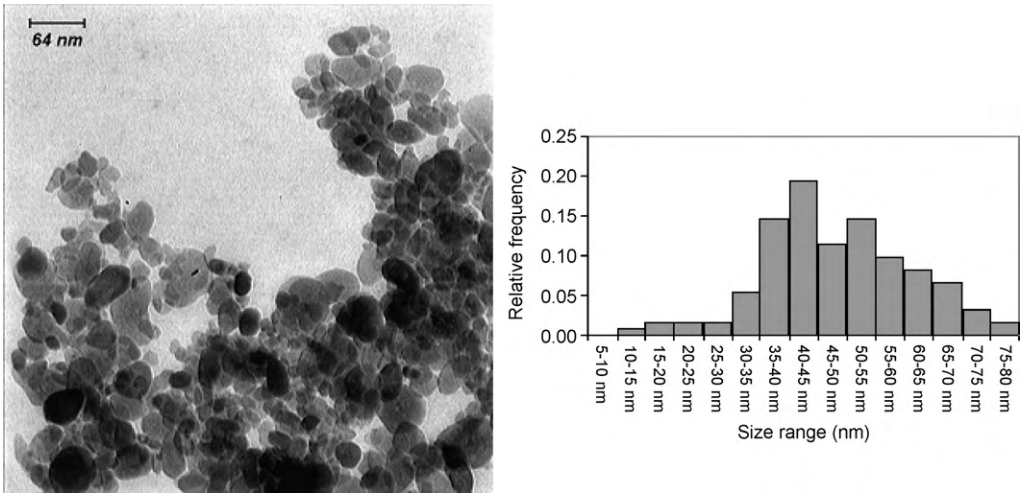

Fig. 12. TEM image and relative particle size distribution of bulk catalyst samples after 105 h time-on-stream (TOS) reaction. Reaction conditions: 563 K, $H_2/CO = 1$, 1.7 MPa, $SV = 4.9\ nl\ h^{-1}\ g_{Fe}^{-1}$, TOS = 105 h.

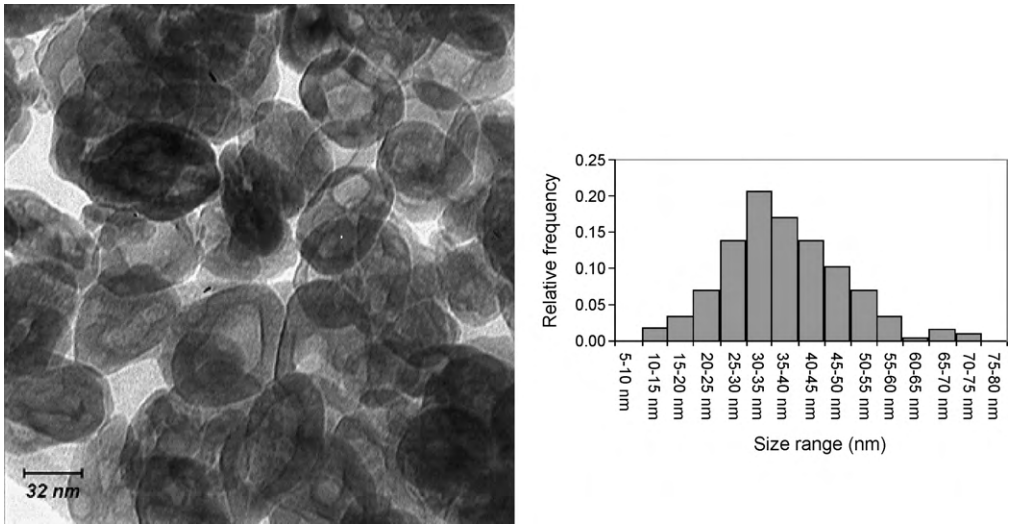

Fig. 13. TEM image and relative particle size distribution of microemulsion catalyst samples after 105 h time-on-stream (TOS) reaction. Reaction conditions: 563 K, $H_2/CO = 1$, 1.7 MPa, SV = 4.9 nl h^{-1} g_{Fe}^{-1}, TOS = 105 h.

for conventional bulk catalyst is much spread and almost in the range between 15 and 60 nm. The TEM image of the used catalyst sample collected after FTS reaction for 105 h is shown in Figs. 12 and 13. Figure 11 reveals an increase in the particle size during Fischer–Tropsch synthesis.

Recently, Murzin reported that FTS reaction is assize-depended heterogeneous catalytic reaction and FTS activity was changed by catalyst particle size [36]. He proposed a kinetics model for evaluation of catalyst particle size on FTS activity. Thus we concluded that a part of the lost of catalyst activity in FTS reaction may be related to increased in the particle size during reaction.

4. Discussion

The initial activity of the ultrafine iron catalyst was found to be higher in comparison with conventional bulk catalyst, in contrast, deactivation rates of this nano-structured catalyst was higher. These different catalytic activities may be related to catalyst particle size and chemical composition of the sample which plays a key role on the catalytic performance. XRD and TPSR-H_2 results indicate that the main iron carbide produced in nano-catalyst is $\acute{\varepsilon}$-carbide ($Fe_{2.2}C$). Pervious results suggest that the $\acute{\varepsilon}$-carbide ($Fe_{2.2}C$), which produced more than Hägg carbide (χ-$Fe_{2.5}C$) and cementite (θ-Fe_3C) in iron nano-particles after pretreatment, is the most catalytic active phase in FTS reaction [8,9,37].

Xu and Bartholomew [19] concluded that the C_α is the most reactive carbon deposited on the surface of the catalyst. High amounts of this species caused higher initial activity of the catalysts after pretreatment. We concluded that the high initial activity of nano-structured catalyst attributes to more carbon-rich $\acute{\varepsilon}$-$Fe_{2.2}C$ carbides and higher concentration of C_α carbonaceous species. Deactivation rate of the catalysts is an opposite scenario with initial catalyst activity. Nano-structured iron catalyst has more deactivation rate and it has been tried to contribute these changes in catalyst activity to variation of catalyst composition.

Eliason and Bartholomew [6] proposed two deactivation paths while occurring in parallel and/or coupled. In this model, adsorbed α-carbon atoms condensed and polymerized to amorphous β-carbon followed to graphitic δ-carbons, and/or in parallel route α-carbon atoms would be precipitated in the transformation of carbon-rich $\acute{\varepsilon}$ to more iron-rich χ and θ phases progressively. These iron carbides transformation increase thermal stability for carbides is $\acute{\varepsilon} < \chi < \theta$; presumably Fe–C bond strength increases in the same order. Thus, the activity of iron carbides in hydrogenation of the surface atomic carbon and then FTS activity order is $\acute{\varepsilon} > \chi > \theta$ [8,9,37]. Therefore, observed losses of iron catalyst activity are attributed to the transformation of the active carbons into inactive carbons and active carbides into lower active carbides. XRD and TPSR-H_2 results for used catalyst shows high amounts of more iron rich cementite (θ-Fe_3C) and inactive graphite-type species, which are thermodynamically stable under oxidizing atmosphere in FTS reaction.

Sarkar et al. [11] reported that particle size distribution (PSD) measurements indicate growth of individual catalyst particles. The breadth, mode and median of PSD were found to increase continuously with time-on-stream of FTS reaction. Recently, Murzin reported that an FTS reaction rate was changed by catalyst particle size and decreased with increasing of catalyst particle size [36].

Based on Bartholomew et al. and Murzin results, we concluded that the deactivation of used catalysts contributes into three paths: growth of individual catalyst particles, condensation of adsorbed α-carbon atoms to amorphous β-carbon followed to graphitic δ-carbons, and/or in parallel route α-carbon atoms would be precipitated in the transformation of carbon-rich $\acute{\varepsilon}$ to more iron-rich χ and θ phases progressively. But the amount of the graphite-type species observed in TPSR-H_2 is higher than our expectation. It has been concluded that another route exists in production of graphite-type species. Jung and Thomson [38] speculated that carbon atoms precipitated by the $\acute{\varepsilon}$ to χ transformation might serve nucleation sites for Boudouard reaction:

$$2CO \rightarrow CO_2 + C_s \quad (8)$$

The Reitmeier et al. [39] calculation shows that the main contributor to carbon deposition is CO disproportionation. Then it has been considered another deactivation path in activity loss of iron catalyst in FTS reaction while occurring in parallel coupled with other two paths.

It has been concluded that the deactivation of the catalyst occur into four paths: first, condensation of adsorbed α-carbon atoms to amorphous β-carbon followed to graphitic δ-carbons; second, in parallel route, α-carbon atoms would be precipitated in the transformation of carbon-rich $\acute{\varepsilon}$ to more iron-rich χ and θ phases progressively; third, route graphite-type species is produced from CO disproportionation, and final, the growth of catalyst particle size due to agglomeration of produced iron carbides during FTS reaction.

5. Conclusion

Bulk iron phase compositions and phase transformations of carbonaceous species during pretreatment and following reaction were characterized using temperature-programmed surface reaction with hydrogen (TPSR-H_2) and XRD techniques. These results indicate that content of carbon-rich $\acute{\varepsilon}$-carbides and C_α carbons (atomic carbonaceous species) after pretreatment enhanced in nano-structured size iron catalyst. It has been concluded that the deactivation of the catalysts occur into four paths: condensation of adsorbed α-carbon atoms to amorphous β-carbon followed to graphitic δ-carbons; in parallel route, α-carbon atoms would be precipitated in the transformation of carbon-rich $\acute{\varepsilon}$ to more iron-rich χ and θ phases progressively; route graphite-type species is produced from CO disproportionation and the growth of catalyst particle size.

References

[1] R.B. Anderson, The Fischer–Tropsch Synthesis, Academic Press, Orlando, FL, 1984.
[2] M.E. Dry, The Fischer–Tropsch synthesis, in: J.R. Anderson, M. Boudart (Eds.), Catalysis, Science and Technology, Springer-Verlag, New York, 1981, p. 159.
[3] C.H. Bartholomew, Recent Developments in Fischer–Tropsch Catalysis, New Trends in CO Activation, Studies in Surface Science and Catalysis, No. 64, Elsevier, Amsterdam, 1991.
[4] G.P. van der Laan, A.A.C.M. Beenackers, Catal. Rev. Sci. Eng. 41 (1999) 255.
[5] F.J. Farrauto, C.H. Bartholomew, Introduction to Industrial Catalytic Processes. Fundamentals and Practice, Chapman & Hall, London, 1997 (Chapter 6).
[6] S.A. Eliason, C.H. Bartholomew, in: C.H. Bartholomew, G.A. Fuentes (Eds.), Catalyst Deactivation, Elsevier, Amsterdam, 1997, p. 517.
[7] S.A. Eliason, C.H. Bartholomew, Appl. Catal. A 186 (1999) 229.
[8] A. Nakhaei Pour, S.M.K. Shahri, Y. Zamani, M. Irani, S. Tehrani, J. Nat. Gas Chem. 17 (2008) 242.
[9] J.A. Amelse, J.B. Butt, L.H. Scwartz, J. Phys. Chem. 82 (1978) 558.
[10] T. Riedel, H. Schulz, G. Schaub, K.W. Jun, J.S. Hwang, K.W. Lee, Top. Catal. 26 (2003) 41.
[11] A. Sarkar, D. Seth, A.K. Dozier, J.K. Neathery, H.H. Hamdeh, B.H. Davis, Catal. Lett. 117 (2007) 1.
[12] P.H. Emmett (Ed.), Crystallite Phase and Their Relationship to Fischer–Tropsch Catalysis, Reinhold, New York, 1956, p. 407.
[13] T. Herranz, S. Rojas, F.J. Peĭrez-Alonso, M. Ojeda, P. Terreros, J.L.G. Fierro, J. Catal. 243 (2006) 199.
[14] W. Ning, N. Koizumi, H. Chang, T. Mochizuki, T. Itoh, M. Yamada, Appl. Catal. A 312 (2006) 35.
[15] S. Li, R.J. O'Brien, G.D. Meitzner, H. Hamdeh, B.H. Davis, E. Iglesia, Appl. Catal. A 219 (2001) 215.
[16] J.W. Niemantsverdriet, A.M. van der Kraan, W.L. van Dijk, H.S. van der Baan, J. Phys. Chem. 84 (1980) 3363.
[17] D.J. Dwyer, J.H. Hardenbergh, J. Catal. 87 (1984) 66.
[18] A. Loaiza-Gil, B. Fontal, F. Rueda, J. Mendialdua, R. Casanova, Appl. Catal. A 177 (1999) 193.
[19] J. Xu, C.H. Bartholomew, J. Phys. Chem. B 109 (2005) 2392.
[20] A. Nakhaei Pour, S.M.K. Shahri, H.R. Bozorgzadeh, Y. Zamani, A. Tavasoli, M.A. Marvast, Appl. Catal. A 348 (2008) 201.
[21] A. Nakhaei Pour, S.M.K. Shahri, Y. Zamani, A. Zamanian, J. Nat. Gas Chem. 19 (2010) 193.
[22] A. Nakhaei Pour, M.R. Husiandoukht, S.F. Tayyari, J. Zarkesh, M.R. Alaei, J. Nat. Gas Sci. Eng. 2 (2010) 61.
[23] H. Hayashi, L.Z. Chen, T. Tago, M. Kishida, K. Wakabayashi, Appl. Catal. A 231 (2002) 81.
[24] X. Li, B. Zhong, S. Peng, Q. Wang, Catal. Lett. 23 (1994) 245.
[25] T. Herranz, S. Rojas, F.J. Peĭrez-Alonso, M. Ojeda, P. Terreros, J.L.G. Fierro, Appl. Catal. A 311 (2006) 66.
[26] S. Eriksson, U. Nyleĭn, S. Rojas, M. Boutonnet, Appl. Catal. A 265 (2004) 207.
[27] M.J. Schwuger, K. Stickdorn, R. Schomacker, Chem. Rev. 95 (1995) 849–864.
[28] C. Liu, B. Zou, A.J. Rondinone, Z.J. Zhang, J. Phys. Chem. B 104 (2000) 1141.
[29] A. Nakhaei Pour, S. Taghipoor, M. Shekarriz, S.M.K. Shahri, Y. Zamani, J. Nanosci. Nanotechnol. 9 (2009) 4425.
[30] A. Nakhaei Pour, M.R. Husiandoukht, S.F. Tayyari, J. Zarkesh, J. Nat. Gas Chem. 19 (2010) 284.
[31] A. Nakhaei Pour, M.R. Husiandoukht, S.F. Tayyari, J. Zarkesh, J. Nat. Gas Chem. 19 (2010) 107.
[32] A. Nakhaei Pour, M.R. Husiandoukht, S.F. Tayyari, J. Zarkesh, J. Nat. Gas Chem. 19 (2010) 333.
[33] A. Nakhaei Pour, M.R. Husiandoukht, J. Zarkesh, S.F. Tayyari, J. Nat. Gas Sci. Eng. 2 (2010) 79.
[34] M.D. Shroff, A.K. Datye, Catal. Lett. 37 (1996) 101.
[35] S. Li, A. Li, S. Krishnamoorthy, E. Iglesia, Catal. Lett. 77 (2001) 197.
[36] D.Y. Murzin, J. Mol. Catal. A, 315 (2010) 226.
[37] R.T. Obermyer, L.N. Mulay, C. Lo, M. Oskooie-Tabrizi, V.U.S. Rao, J. Appl. Phys. 53 (1982) 2683.
[38] H. Jung, W.J. Thomson, J. Catal. 134 (1992) 654–667.
[39] R.E. Reitmeier, K. Atwood, H.A. Bennet, H.M. Baugh, Ind. Eng. Chem. 40 (1998) 620.